Downloaded from https://academic.oup.com/mnras/article/521/4/5624/7083162 by Gary Ives user on 29 October 2023

MNRAS **521**, 5624–5635 (2023) Advance Access publication 2023 March 21

Sky-brightness measurements in J, H, and Ks bands at DOME A with NISBM and early results

Jun Zhang, ¹*† Yi-hao Zhang, ¹† Qi-Jie Tang, ¹† Jian Wang, ¹* Peng Jiang, ²* Michael C. B. Ashley, ³ Tuo Ji, ² Shao-hua Zhang ⁹, ⁴ Qi Feng, ¹ Zhi-yue Wang, ¹ Feng Zeng, ¹ Hong-fei Zhang, ¹ Jin-ting Chen, ¹ Jie Chen, ¹ Ming-hao Jia, ¹ Guang-yu Zhang, ¹ Hong-yan Zhou, ^{5,2} Yi hu ⁹, ⁶ Lifan Wang ⁷ and Qing-feng Zhu⁵

Accepted 2023 March 10. Received 2023 March 7; in original form 2022 December 30

ABSTRACT

The radiance of sky brightness differs principally with wavelength passband. Atmospheric scattering of sunlight causes the radiation in the near-infrared band. The Antarctic is a singular area of the planet, marked by an unparalleled climate and geographical conditions, including the coldest temperatures and driest climate on Earth, which leads it to be the best candidate site for observing in infrared bands. At present, there are still no measurements of night-sky brightness at DOME A. We have developed the Near-Infrared Sky Brightness Monitor (NISBM) in the J, H, and H is bands for measurements at DOME A. The instruments were installed at DOME A in 2019 and early results of NIR sky brightness from 2019 January–April have been obtained. The variation of sky background brightness with solar elevation and scanning angle is analysed. The zenith sky flux intensity for the early night at DOME A in the H band is in the 600–1100 μ Jy arcsec⁻² range, that in the H band is between 1100 and 2600 μ Jy arcsec⁻², and that in the H band is in the range \sim 200–900 μ Jy arcsec⁻². This result shows that the sky brightness in H bands is close to that of Ali in China and Mauna Kea in the USA. The sky brightness in the H band is much better than that in Ali, China and Mauna Kea, USA. This shows that, from our early results, DOME A is a good site for astronomical observation in the H band.

Key words: site testing – instrumentation: photometers – methods: observational.

1. INTRODUCTION

Night-sky brightness in the near-infrared (NIR) is a crucial aspect of observatory operations, essential for the design of near-infrared instruments and scientific studies. Earth's atmosphere blocks most infrared radiation from celestial objects, yet there are several windows of wavelength bands where ground-based infrared astronomical observations can still be conducted. In the NIR wavelength bands, there are J, H, K, L, and M windows, as shown in Fig. 1.

The filter sets used at Mauna Kea and the South Pole are listed in Table 1. The 'Mauna Kea' part of Table 1 list the filter sets that have been used for many years at the listed observatories on Mauna Kea, which are the National Aeronautics and Space Administration (NASA), the Infrared Telescope Facility (IRTF), the United King-

dom Infrared Telescope (UKIRT), and the Canada–France–Hawaii Telescope (CFHT: Simons 2002). The column, 'Barr', lists the Barr Associates standard astronomy filter sets. After summarizing the commonalities in the filters of these observatories, some optimal J, H, K', Ks, L, and M filters are defined in 'MKO-NIR' column (Simons 2002; Tokunaga 2002), which provide better photometric linearity and reduced background, as well as preserving good throughput within the J, H, K, L, and M atmospheric windows.

For infrared observations in Antarctica, the 'South Pole' part of Table 1 lists filter sets for two experiments used for background measurements of the Antarctic sky, the instruments used for these experiments being the near-infrared grating spectrometer (GRIM: Nguyen 1996) and the infrared photometer spectrometer (IRPS: Ashley 1996).

Many renowned astronomical observatories have monitored nearinfrared sky brightness for a long time. A bright sky significantly reduces the capabilities of astronomical telescopes and instruments in the NIR spectrum, in areas such as the magnitude of observed stars, depth of sky surveys, and duration of apparatus exposure.

¹ State Key Laboratory of Particle Detection and Electronics, Department of Modern Physics, University of Science and Technology of China, Hefei 230026, China

²Key Laboratory for Polar Science, MNR, Polar Research Institute of China, Shanghai, China

³School of Physics, University of New South Wales, Sydney, New South Wales, Australia

⁴Shanghai Key Lab for Astrophysics, Shanghai Normal University, Shanghai 200234, China

⁵Department of Astronomy, University of Science and Technology of China, Hefei 230026, China

⁶National Astronomical Observatories, Chinese Academy of Sciences, Beijing, China

⁷Texas A&M University, College Station 77845, TX, USA

^{*}E-mail: zj2018@mail.ustc.edu.cn (JZ); wangjian@ustc.edu.cn (JW); Jiangpeng@pric.org.cn (PJ)

[†] Jun Zhang, Yi-hao Zhang, and Qi-jie Tang contributed equally to this work.

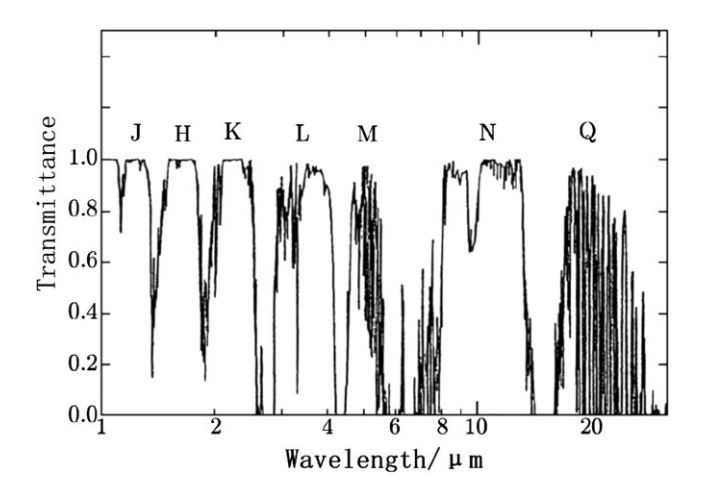


Figure 1. Atmospheric transmission rates in the near-infrared band and definitions for each passband.

The radiance of sky brightness varies primarily according to the wavelength passband. In the NIR band, the radiation is caused by atmospheric scattering from sunlight. The high Antarctic plateau has special geographic and meteorological conditions that make it a unique place on Earth, i.e. the coldest and driest. The central Antarctic plateau is considered the best place on Earth for infrared (IR) observations. Now many countries have established scientific stations on the mainland of the Antarctic. Some measurements of near-infrared sky brightness have been carried out, including at the South Pole and Ridge A (Ashley 1995; Phillips 1999; Storey 1999; Matthew 2018), which are known to possess some conditions that are better than those at mid-latitude sites like Mauna Kea, Siding Spring, Paranal, Calar Alto, and Mount Hamilton. Table 2 lists some of the published approximate ranges of nightsky brightness provided in the literature and on the web pages of different observatories. The data gathered from these measurements could be immensely useful for the design and construction of future infrared telescopes and instruments and could have a significant impact on researchers and policymakers in the creation of new observatories.

At DOME A, Ma (2020) measured the night-time seeing, but at that time no such measurements were available for NIR sky brightness (Shang 2020). For the mission of measurement at DOME A, Tang (2018) developed a near-infrared sky-brightness monitor (NISBM) using InGaAs detectors and conducted field measurements at Ngari

Observatory, Tibet. After revision of the NISBM to run in extreme cold-temperature and high-latitude environments, the instrument was carried to DOME A by the 35th Chinese National Antarctic Research Expedition team and installed and run successfully in 2019 January.

The rest of the work is organized as follows. Section 2. introduces the instruments making up the NISBM for DOME A. Section 3. describes the calibration of the instrument. Section 4. describes the deployment at DOME A and observations made and discusses the first results.

2. NISBM FOR DOME A

The observation range of he NISBM covers the *J*, *H*, and *K*s bands, and three sets of filters and detectors have been selected for each band. The *J*, *H*, and *K*s filters used in the NISBM for DOME A are purchased from Asahi Spectra and manufactured according to the MKO (Mauna Kea Observatory) filter specifications (Tokunaga 2002), which are shown in Table 3. The cut-on and cut-off wavelengths are where the filter transmittance is 50% of its peak. The transmittance curves of the three filters are shown in Fig. 2.

For the selection of detectors, we take several commonly used NIR detectors into consideration: for example InGaAs, InSb, and HgCdTe (MCT). The parameters of these detectors, such as detection rate (*D**), noise (NEP), dark current, and operating temperature, are investigated fully, as shown in Table 4. According to Table 4, in the *J*, *H*, and *K*s bands, the InGaAs detector stands out for its higher *D**, lower NEP, and lower dark current at 233 K. For InSb or HgCdTe detectors, a refrigerator or liquid nitrogen is required to achieve a low temperature of 77 K to reduce the dark current of the detectors, which makes the instrument design more complex (Ashley 1995).

Furthermore, in measurements at the South Pole with the NISM in the $K_{\rm dark}$ window, a leakage of approximately 0.01% from 2.5–5 μ m is discovered, due to filter leakage in this wavelength band (Lawrence 2002), which is called 'long-wavelength leakage'. With the rapidly increasing flux at these wavelengths, even a very small amount of leakage in the filter will lead to an obvious signal in the detectors, which may overlap the measured signal, although the filter transmittance was calibrated and the sky spectral brightness in the $K_{\rm dark}$ band was obtained by complex analysis and correction (Lawrence 2002). From Fig. 3, it is clear that red leakage of the J-band filter appears at 2.9 μ m. As for the cut-off wavelengths of the InSb detector and the HgCdTe detector at 5.5 μ m, red leakage of the filter makes the detector more susceptible. The cut-off wavelength of the InGaAs detector is located at 1.6 μ m and it cannot sense a

Table 1. Filter sets used at Mauna Kea and the South Pole.

Filter						
	UKIRT ⁽¹⁾	IRTF ⁽¹⁾	Mauna Kea CFHT ⁽¹⁾	Barr ⁽²⁾	MKO-NIR ⁽²⁾	South Pole IRPS ⁽²⁾ , GRIM ⁽²⁾
\overline{J}	1.13-1.42	1.11–1.42	1.10-1.39	1.11–1.39	1.17-1.33	1.08-1.32
H	1.13-1.42	1.48-1.76	1.51-1.79	1.50-1.80	1.49-1.78	1.51 - 1.79
K	2.00-2.41	2.02-2.41	2.02-2.41	2.00-2.40	2.03-2.37	1.99-2.41
K'	_	1.95-2.29	1.95-2.29	_	1.95-2.29	1.94-2.29
$K_{\rm s}$	1.99-2.32	1.99-2.31	_	_	1.99-2.31	_
$K_{\rm dark}$	_	_	_	_	_	2.27-2.45
L	3.15-3.75	3.20-3.81	_	3.20-3.80	_	2.90-4.10
L'	3.50-4.10	3.49-4.08	_	3.50-4.10	3.42-4.12	_
M	_	4.54-5.16	_	4.50-5.10	_	4.60-5.00
M'	4.55-4.80	4.67-4.89	_	_	4.57-4.79	_

Notes: (1) The cut-on (λ_1) and cut-off (λ_2) wavelengths correspond to where the transmission is 10% of the peak. (2) The cut-on (λ_1) and cut-off (λ_2) wavelengths correspond to where the transmission is 50% of the peak.

Table 2. Flux intensities of various NIR bands.

Sites	Altitude	Intensity (μ Jy arcsec ⁻²)					
		J	H	K	K_{s}	K_{dark}	
South Pole ⁽¹⁾	2800	~300–600	~800–2000	~300–700	~400	~150-300	
Mauna Kea ⁽²⁾	4200	~592	~3262	~767	~843	1000-2000	
Siding Spring ⁽¹⁾	1165	\sim 1000-1500	\sim 1500 $-$ 3000	\sim 6000–15000	~3000–7000	~4000	
Paranal ⁽³⁾	2635	~409	~1877	_	~2500-4300	_	
Calar Alto ⁽⁴⁾	2168	~268	~1100	~7393	~ 2547	_	
Mount Hamilton ⁽⁵⁾	1283	~649	~ 2700	_	~4000	_	
-60° , 5% emission	_	8×10^{-11}	2×10^{-5}	5×10^{-2}	2×10^{-1}	7×10^{-1}	

Notes: (1)refers to the zenith flux intensity reported by Philips (1999) and Lawrence (2002); (2)refers to Gemini Observatory Web, http://www.gemini.edu/observing/telescopes-and-sites/sites#Near-IR-short; (3)refers to Paranal Observatory Web, http://www.eso.org/gen-fac/pubs/astclim/paranal/skybackground/; (4) refers to Sánchez (2008); (5) refers to User's Guide to IRCAL, https://mthamilton.ucolick.org/techdocs/instruments/ircal/ircal_detector.html#-%20sky . The final row gives, from Phillips (1999), for comparison, the flux from a greybody at -60° C (the average wintertime temperature in the Antarctic) and 5% emissivity.

Table 3. Specifications of *J*, *H*, and *K*s filters used for NISBM.

Band	Centre (µm)	Cut-on (µm)	Cut-off (µm)
\overline{J}	1.250	1.170	1.330
H	1.635	1.490	1.780
Ks	2.150	1.990	2.310

red leakage wavelength. In combination with the above, the InGaAs detector has unparalleled advantages in detecting the J, H, and Ks bands, and different models of InGaAs detectors for each band are selected, as shown in Fig. 4. The InGaAs detectors purchased from Hamamatsu are divided into standard and wavelength-extended models, covering a range from 0.5–2.6 μ m. As shown in Fig. 4, G12180 with a cut-off wavelength at 1.65 μ m is chosen for the J-band measurement, G12182 with a cut-off wavelength at 2.05 μ m is chosen for measurement in the H band, and G12183 with a cut-off wavelength at 2.55 μ m is chosen for measurement in the H band.

The design of the first version of the NISBM was finished in 2017, and a field measurement of *J*, *H*, and *K*s bands at Ali Observatory, Tibet was conducted (Tang 2018). Owing to the extreme climate conditions of DOME A in Antarctica, such as low temperature, low air pressure, high altitude, snow cover, and frost, a refined version of the NISBM for Dome A is introduced in this work.

The NISBM consists of three independent radiation meters used separately to measure the sky background intensity of the three bands *J*, *H*, and *K*s at the Kunlun Station in DOME A, Antarctica. The mechanics of each meter is shown in Fig. 5 and its function diagram is shown in Fig. 6. To make sure the NISBM works well in the extreme temperatures of Antarctica, moving components like a filter wheel, line variable filter (LVF), and circular variable filter (CVF) are not used because of their easy failure (Ashley1995; Chen 2020). Furthermore, if one meter fails, the other two can still conduct their measurement unattended. The three-band meters can also work paralleled, which leads to more efficiency.

Each meter of the NISBM for DOME A consists of a scanning mirror, an optical lens group, a chopper, a filter, a detector module, an electronic control module, and a data acquisition module, as shown in Fig. 6. A gradienter is used for horizontal adjustment and a compass is used for the angle measurement of each device. The scanning mirror, for scanning the sky with different altitude angles, is mainly composed of a mirror, a driving motor, and an angle sensor. The mirror is critical because its reflectivity in the infrared band is the key index. Low reflectivity contributes to higher emissivity of the mirror and self-induced infrared radiation, which significantly affects the weak sky-brightness signal and the optical efficiency, especially in the measurement of longer wavelength radiation. The average reflectivity of the gold-coated mirror reaches 96 per cent in the range 800 nm— $20 \mu \text{m}$. The optical lens group gathers the parallel light

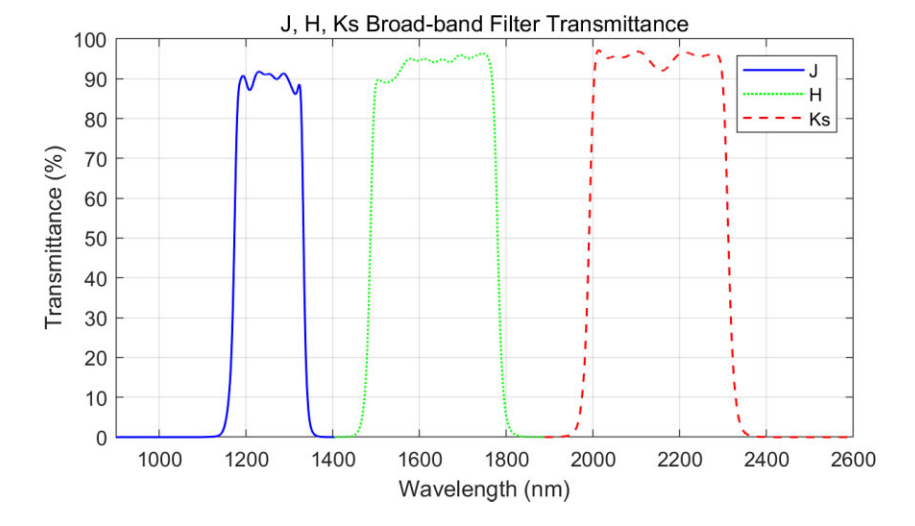


Figure 2. Transmittance curves of *J*, *H*, and *K*s wide-band filters.

 1.1×10^{-12}

10000

InSb HgCdTe Detector InGaAs Judson Tec. Manufacturer Hamamatus Judson Tec. Model G12183-220K J10D-M204-R02M-60 J15D5-M204-S01M-60 0.9 - 2.55Wavelength range (μ m) 1.0 - 5.52 - 5.5Operating temperature (K) 233-358 77 77 4.5×10^{11} at 253 K 1×10^{11} $8\!\times\!10^{10}$ $D* (\text{cm Hz}^{1/2} \text{ W}^{-1})$

 1.6×10^{-12}

30

 4×10^{-13} at 253 K

2.1

Table 4. Characteristics of detectors InGaAs, InSb, and HgCdTe.

NEP (W/Hz^{1/2}) Dark current (μA)

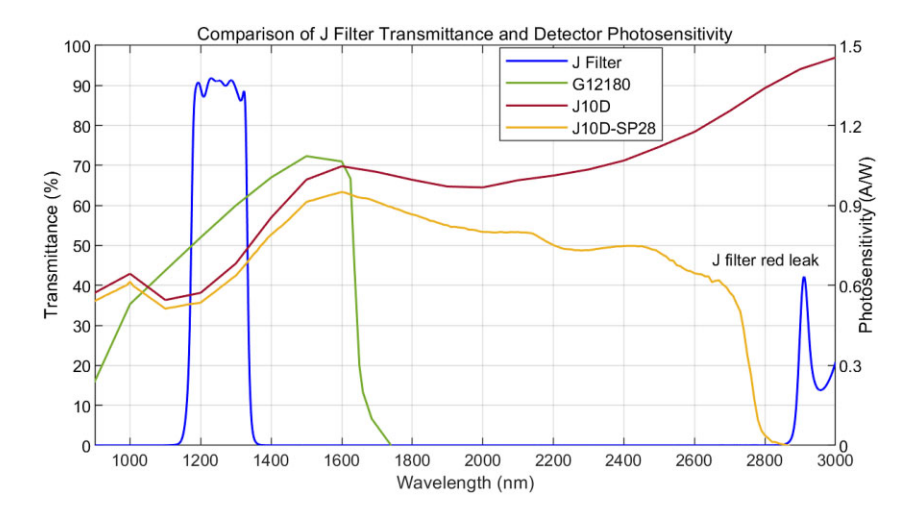


Figure 3. Comparison of *J* filter transmittance and detector photosensitivity (G12180 is an InGaAs detector; J10D is an InSb detector; J10D-SP28 is a J10D detector with SP28 cut-off filter).

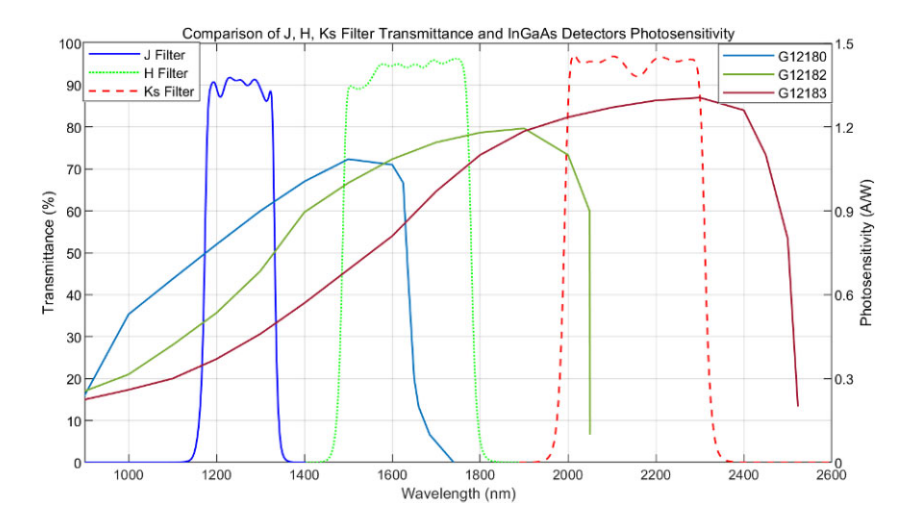


Figure 4. Comparison of the transmittance of the filter and the sensitivity of InGaAs detectors in *J*, *H*, and *K*s bands.

from the scanning mirror to the detector. The optical system for the J (\sim 1.17–1.33 μ m), H (\sim 1.49–1.78 μ m), and Ks (\sim 1.99–2.31 μ m) bands can meet the requirements by using a single aspheric lens, which simplifies the design and realizes a coaxial optical system with high imaging quality (Tang 2019). A chopper works as an optical modulator to modulate the slowly changing DC radiation signal into an AC signal with a fixed frequency. This modulation eliminates or restrains the influence of device background irradiation, detector baseline drift, and operational amplifier low-frequency noise

in sky radiation measurements. The signal-to-noise ratio is greatly improved. The data acquisition module converts and amplifies the current signal from the detector into a voltage signal, demodulates the modulated signal with a lock-in amplifier (LIA), digitizes it with an analogue-to-digital converter (ADC), and obtains the infrared light intensity of the sky after calculation (Tang 2019).

Considering the low temperature and low air pressure at DOME A, the material of all components should be adaptable to a low-temperature environment. For instance, Invar is chosen to build the

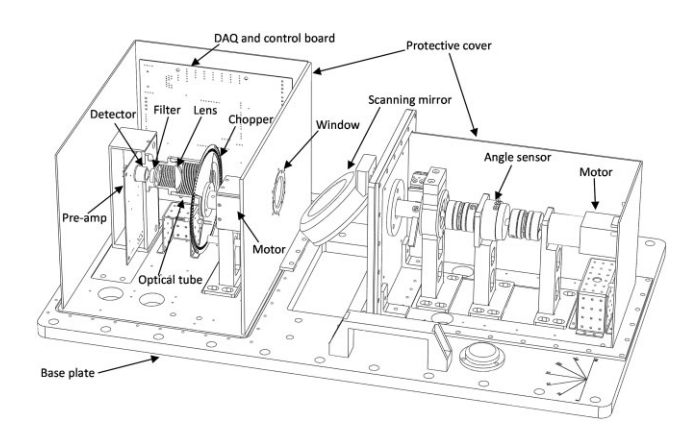


Figure 5. Mechanics of NISBM for DOME A.

optical tube because of its low-temperature deformation coefficient, which improves the energy-gathering efficiency at low temperature. To prevent the influence of water vapour on window glass and optical components at low temperature, all other components are sealed up by a protective cover, except the scanning mirror. The cover is equipped with a built-in desiccant box and filled with nitrogen to prevent the infiltration of water vapour during long-distance transportation to Antarctica. Besides this, the inner surface of the protective cover is affixed with thermal insulation cotton, which maintains the working temperature of the components in the protective cover. Furthermore, thermal insulation and a heater are installed outside the chopper motor, which is manufactured with low thermal expansion coefficient materials and is well lubricated. In our instruments, making the motor run smoothly is very important.

By examining the temperature and humidity data obtained at Kunlun Station, it is found that, unlike the dry air at the low-altitude Zhongshan Station, the air humidity at Kunlun Station, located at a high altitude, is saturated most of the time. As soon as the scanning mirror and sealing window glass are exposed to the atmosphere, frost will be generated immediately, significantly affecting the evaluation of sky brightness. Therefore, a heater is designed and attached to the scanning mirror and the sealing window to make their temperature slightly higher than the ambient temperature by $\sim 3-5~{\rm ^{\circ}C}$. Meanwhile, the heating apparatus can also be used for snow removal.

Considering that all equipment depends on the limited power generated by diesel generators during the polar night, a low-power dissipation design is essential. The total power dissipation of the NISBM, including the three sky-brightness measurement devices in the J, H, and Ks bands, an on-site active blackbody, and an industrial computer crate, is controlled to within 100 W.

Due to the unique geographical conditions of the Antarctic interior, the measured data can only be transmitted back by the *Iridium* satellite network. Because of low bandwidth, high latency, and high cost, an unattended autonomous operation and a reliable network communication system are required. Therefore, efficient remote automatic control software was designed (Wang 2019).

Aside from the extremely low temperature at DOME A, the rarefied atmosphere intensifies solar radiation transmittance. Therefore, it is necessary to arrange the running strategy of the instrument according to the solar altitude angle and time to prevent direct reflection of sunlight into the detector, which could result in irreparable damage. Fig. 7 shows sunrise and sunset times in Kunlun Station over a year, provided by the time and date website

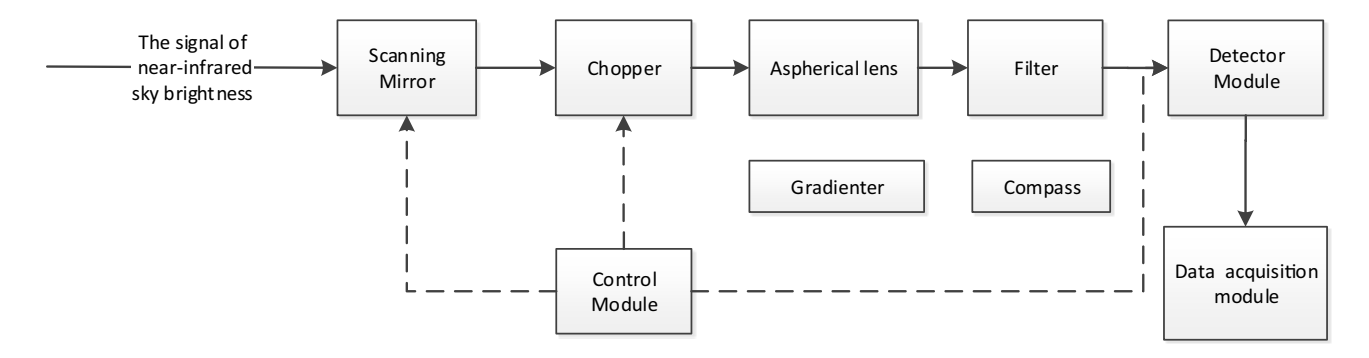


Figure 6. Function diagram of each device of NISBM in *J*, *H*, *K*s bands.

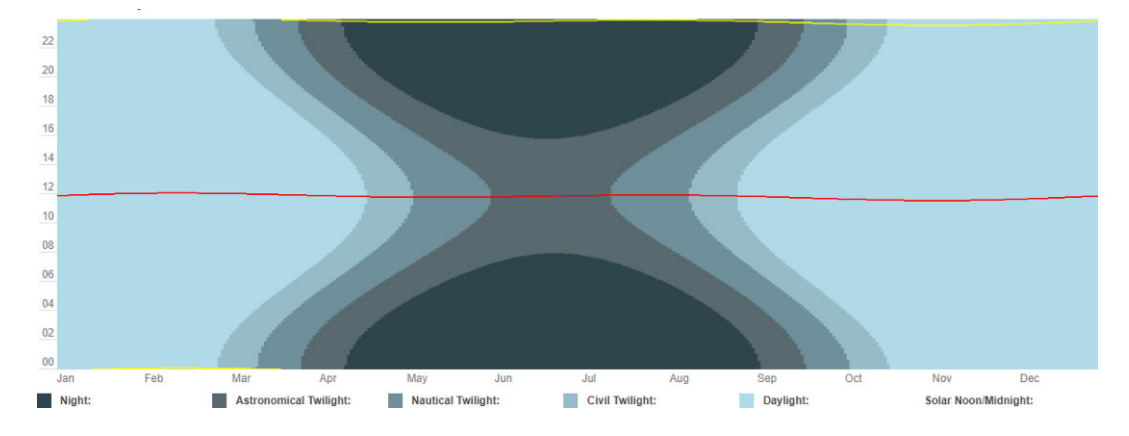


Figure 7. Sunrise and sunset times at DOME A.

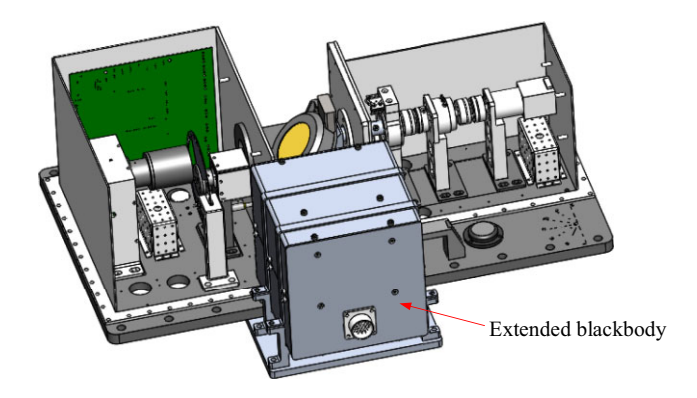


Figure 8. Diagram of *K*s-band radiation meter.

(https://www.timeanddate.com). According to the altitude angle and light intensity of the Sun, the period can be divided into night, astronomical twilight, nautical twilight, civil twilight, and daylight. On March 3, five-month daylight ended at DOME A and the equipment began to run. The solar altitude angle can be calculated according to the specific date and time, which can maximize the angle range measured without being illuminated directly by the Sun.

The K band includes some thermal-infrared radiation, which means the K band is easily affected by temperature. This effect is noticeable in the Ks band, particularly because of thermal radiance from the chopper vanes, which cannot be ignored. Therefore, an actively extended blackbody is equipped for on-site calibration to correct the impact of the ambient temperature fluctuation. The active blackbody is an extended blackbody with active heating capability, located at 180° pointing position of the Ks-band device. With accurate temperature measurement and control, the blackbody surface can be stabilized at a temperature higher than the ambient temperature (stability \pm 0.015 °C). The blackbody provides a constant signal source and is visible in every sweep of the Ks-band meter. The measured data from each scan can be calibrated by the blackbody. The Ks-band radiation meter with an actively extended blackbody is shown in Fig. 8.

3. CALIBRATION

Calibration of the NISBM is critical for an accurate infrared measurement, which is achieved using a calibrated blackbody. The primary method of calibration is described in Tang et al. (2018)), and the *K*sband monitor is equipped with an active blackbody for calibration. As shown in Fig. 9, the effective radiating temperature of the chopper leads to the bulk of the background radiation of the NISBM, so it affects the accuracy of measurement most.

The chopper is not an ideal blackbody; its emissivity is less than 1. Furthermore, the parameters of the instrument deviate from their real value. To obtain accurate data regarding the relationship between the output current value of the detector and the temperature of a blackbody, blackbody calibration experiments need to be conducted. The real current value $I_{\rm Signal}(T)$ is proportional to the theoretical value $I_{\rm PD}(T)$, the formula for which is

$$I_{\text{Signal}}(T) = aI_{\text{PD}}(T) + b. \tag{1}$$

Here, a is the deviation coefficient of system responsivity and its theoretical value, which is decided by the instrument and not influenced by ambient conditions; b is the offset, which is mainly from the chopper vanes and is influenced by the ambient temperature.

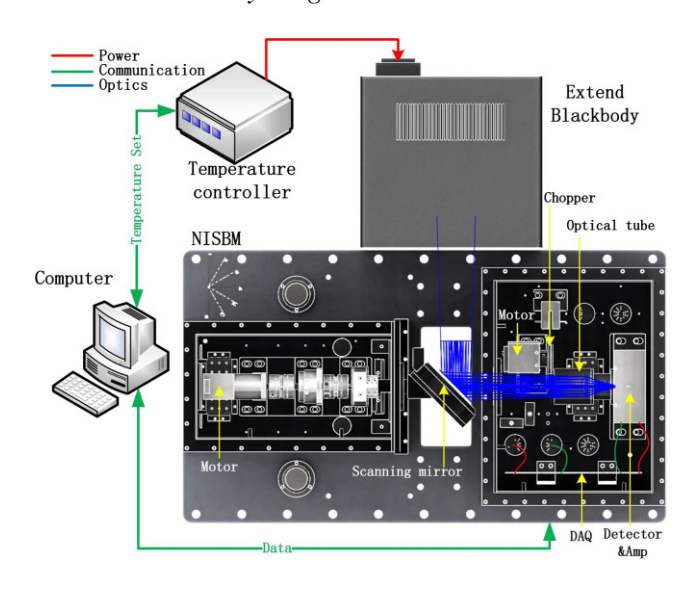


Figure 9. Setup diagram of the blackbody calibration experiment.

Table 5. Fitting coefficients of device for the *J*, *H*, and *K*s bands.

Coefficient	J	Н	Ks
R^2	1	1	1
RMS error	0.01122	0.04738	0.9478
a	0.997 ± 0.003	1.087 ± 0.003	1.205 ± 0.002
b(pA)	-0.01 ± 0.01	-1.40 ± 0.06	-290 ± 1
b Theoretical (pA)	-0.0002	-1.408	-399.1

Both a and b are calibration coefficients obtained from blackbody calibration experiments.

The theoretical value $I_{PD}(T)$ is calculated as

$$I_{\rm PD} \ (T) = \ ASC_{\rm CP} \bar{\eta}_{\rm OPT} \bar{\varepsilon}_{\rm BB} \int\limits_{\lambda_1}^{\lambda_2} w \left(\lambda, T\right) \eta_{FT} (\lambda) \, R \left(\lambda\right) \, {\rm d}\lambda. \tag{2}$$

Here, A is the solid angle, S is the effective entrance pupil area of the optical window, C_{CP} is the ratio of the sinusoidal component and the peak value of the signal, $\bar{\eta}_{\text{OPT}}$ is the total transmission coefficient of the optics, $\bar{\varepsilon}_{\text{BB}}$ is the emissivity of a blackbody, $\eta_{\text{FT}}(\lambda)$ is the transmission of the filters, $R(\lambda)$ is the responsivity of the detector, and λ_1 and λ_2 are the boundaries of the band.

The setup of the blackbody calibration experiment is shown in Fig. 9. An extended blackbody is used to encompass the instrument's scope of vision. Calibration is accomplished by altering the blackbody temperature to provide a variable intensity signal to the detector. The flux can be monitored and recorded once the temperature of the blackbody has been stabilized at a given point. The theoretical current value is calculated with formula (2) according to the parameters of the three instruments for the J, H, and Ks bands. Based on formula (1), the coefficients a and b can be fitted; the fitting results are shown in Table 5.

The result shows that the linearity of the fitting is very good. The coefficient a is close to 1, which means that the theoretical calculation and experimental values match well. The ambient temperature in the experiments was about 27 °C. As shown in Table 5, coefficient b in the J band is almost zero, which means that the background radiation in the J band is very small at room temperature. The coefficient b is 1.40 pA in the H band, which means that the background radiation is also small in this band at room temperature. With a decrease in ambient temperature, the value decreases. The coefficient b in the Ks

Table 6. Results of calibration experiments in the *J*, *H*, and *K*s bands.

Coefficient	J	Н	Ks
a	0.9968	1.087	1.205
$ar{\eta}_{ ext{FT}}$	0.90	0.94	0.95
$\bar{R} (A W^{-1})$	0.83	1.10	1.27
Δf (Hz)	3.087×10^{13}	3.337×10^{13}	2.098×10^{13}
$C (\mu \text{Jy arcsec}^{-2} \text{pA}^{-1})$	86.1	70.0	99.3

band is 290, which means that the background radiation is intense, close to the theoretical analysis, but still has some deviation. For this reason an on-site blackbody is needed to calibrate the *K*s band.

If the average flux density from the sky is L(f), the current output from the detector I_{Signal} can be calculated as

$$I_{\text{Signal}} = aASC_{\text{CP}}\bar{\eta}_{\text{OPT}}\bar{\varepsilon}_{\text{BB}}\bar{\eta}_{\text{FT}}\bar{R}L(f)\Delta f + b, \tag{3}$$

in which $\bar{\eta}_{\rm OPT}$ is the average transmission of the filter, \bar{R} is the average responsivity of the detector, and $\Delta f = f_{\rm cut-on} - f_{\rm cut-off}$ is the frequency range of the filter.

L(f) is calculated by

$$L (f) = \frac{1}{aASC_{\text{CP}}\bar{\eta}_{\text{OPT}}\bar{\varepsilon}_{\text{BB}}\bar{\eta}_{\text{FT}}\bar{R}\Delta f} \cdot (I_{\text{Signal}} - b)$$
$$= C (I_{\text{Signal}} - b), \tag{4}$$

in which C is the calibration coefficient, which is decided by the instrument. The results of calibration experiments in the J, H, and Ks bands are shown in Table 6.

For the Ks band, b cannot be ignored and needs to be corrected by an on-site active blackbody, as shown in Fig. 8. An extended blackbody was employed as a dependable radiation source with known signal intensity, and its emissivity was measured in the laboratory at a steady temperature. In the running of the Ks-band monitor, the extended blackbody was observed every scanning cycle at elevation angles from 60– 100° , as shown in Fig. 8. The difference between the observed sky brightness intensity and the blackbody radiation intensity is the background radiation of the instrument. The calibration cycle is the same as the scanning cycle of the measurement, which is faster than the ambient temperature drift.

4. DEPLOYMENT AND OBSERVATION

The power supply and communication topology of the NISBM for DOME A are shown in Fig. 10 and photographed in Fig. 11 as installed at DOME A, Antarctica.

Three radiation meters for different waveband measurements are connected to the industrial control computer crate through two 30-m cryogenic cables, used separately for power supply and communication. The power supply and network of the industrial control computer crate are fed by a power platform (PLATEAU

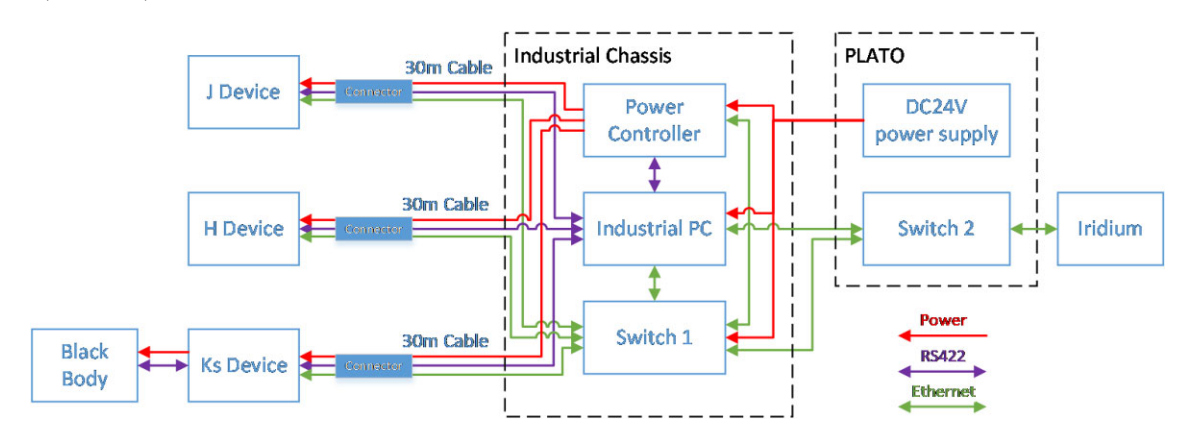


Figure 10. Power supply and communication topology of NISBM for DOME A.



Figure 11. NISBM including three devices installed in DOME A, Antarctica.

Band $J(1.25 \mu m)$ $H(1.635 \mu m)$ $Ks (2.15 \mu m)$ 2.9×10^{-4} 2.8×10^{-3} Attenuation coefficient Sky brightness (μ Jy arcsec⁻²) $2.3 \times 10^{8} - 2.5 \times 10^{8}$ $7.3 \times 10^6 - 1.8 \times 10^7$ $2.5 \times 10^{5} - 4.2 \times 10^{6}$ 2.11 - 2.05Sky brightness (mag arcsec⁻²) 5.4-4.5 8.6-5.5 10.9 Sun elevation (degrees) 29.3 23.8

Table 7. Daytime NIR sky brightness at DOME A, Antarctica (2019 Jan-Feb).

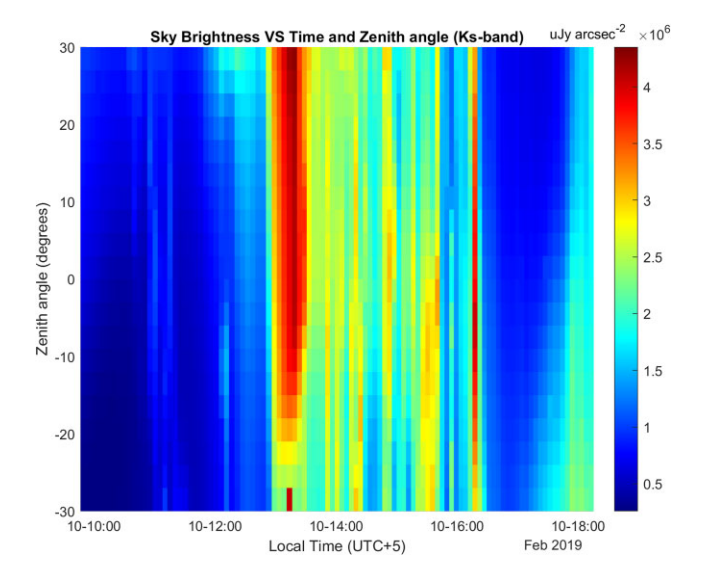


Figure 12. Daytime sky brightness of *K*s band versus time and zenith angle on 2019 February 10.

Observatory, Plato: Lawrence 2009), which provides a DC power supply and realizes data communication through the *Iridium* satellite system. To guarantee the reliability of system communication, RS422 and Ethernet are adopted for local communication simultaneously. The power controller is used to control and monitor the voltage and current of instruments in real time.

After deployment, the system ran for about three months and obtained preliminary measurement data. The results and analysis are given below.

It was summer and daytime at DOME A in 2019 January and February. The sky brightness is too strong to measure for our devices in the J and H bands, and a neutral density filter (NDF) with an OD3 cut-off depth is installed manually on the windows. The NDF is calibrated at our lab. The J-, H-, and Ks-band sky brightness was measured at observational angles from -30° to 30° . The results of the measurements are shown in Table 7. The sky brightness of the Ks band is weaker than that of the J and H bands, and the Ks-band device has a more extensive dynamic range of measurements, so the sky brightness of the Ks band was measured without an NDF. From the results, the measured value of sky brightness in the J and H bands is much higher than that of the theoretical analysis by Yang (2019). According to our inferences and experiments, there is a strong possibility that the installation of the NDF in front of the device window is not conducted well. The NDF in front of the equipment seal window was removed before the Antarctic research crew left, so we only have measurements in the Ks band during the daytime.

As mentioned above, the daytime measurements of the Ks-band monitor without an NDF are valuable. The scanning result of zenith angles from -30° to 30° in the Ks band is shown in Fig. 12. It gives the first daytime measurements of the Ks band after installation. The

intensity of the original sky brightness, in units of μ Jy arcsec⁻², is shown depending on colour, with the colour bar on the right.

From April 15–17, the scanning results of J, H, and Ks bands from elevation angles ranging from -80° to 100° are shown in Fig. 13, which gives the variation of the original sky background intensity in the J, H, and Ks bands at different zenith angles during the transition of DOME A from daytime to night-time.

Some conclusions can be drawn from the data represented in Fig. 13, as follows.

- (1) The sky brightness of all three bands had the lowest value at the zenith. The greater the angle of the Sun, the thicker the atmosphere and the brighter it became.
- (2) The Ks-band measurement taken between 60° and 100° was much lower compared with other readings, as an extended blackbody was present for calibration purposes.
- (3) The values of the J band during 2019 April 15 and 16 are almost same. This may result from a malfunction of the chopper, which is driven by a motor.
- (4) The value of the J band rose sharply due to the effect of solar radiation at 7:00 local time.
- (5) The values for the three devices decreased suddenly at 22:00 local time on April 17. The changes appeared at almost the same time. At that time, based on the value of the *K*s band, the *K*s-band device could still scan the blackbody, which meant the device was running normally. In addition, values of other angles are smaller than those from previous days. We suspect the instruments were either blocked by snow or obscured by thick clouds. From the Kunlun Cloud and Aurora Monitor (KLCAM) at DOME A, shown in Fig. 14, the reason is that it was cloudy from the night of April 17 to the dawn of April 18.

During March and April, daytime turns to night-time at DOME A. In our data, the sky brightness of the *J*, *H*, and *K*s bands at the zenith varied with time, as shown in Fig. 15. The yellow line presents the variance of the Sun's elevation with time. The sky brightness is strongly correlated with the Sun's elevation. At noon, the Sun's elevation is at its maximum. The sky brightness of the three bands is enhanced exponentially and synchronously and reaches its maximum. When the Sun is lower than some elevation, the sky brightness at the zenith is minimally influenced by the Sun's radiation. At this time, the sky is in total darkness, not being illuminated by the Sun's rays. As time goes on, the night-time fraction increases. On April 17, about 12 hours have no direct influence from solar radiation.

The onset time of night differs in different bands because of the different refraction indices at different wavelengths in the atmosphere. The refraction index in the Ks band is less than that in the J band, so the time of entering the night in the Ks band is earlier than that in the J band. Meanwhile, the Sun's elevation in the Ks band is higher than in the J band. The relation between sky brightness at the zenith and the Sun's elevation is analysed, and the results are shown in Fig. 16. The data presented in Fig. 16 have an S-shaped curve, which can be divided into three phases. Between the phases, there are two knee

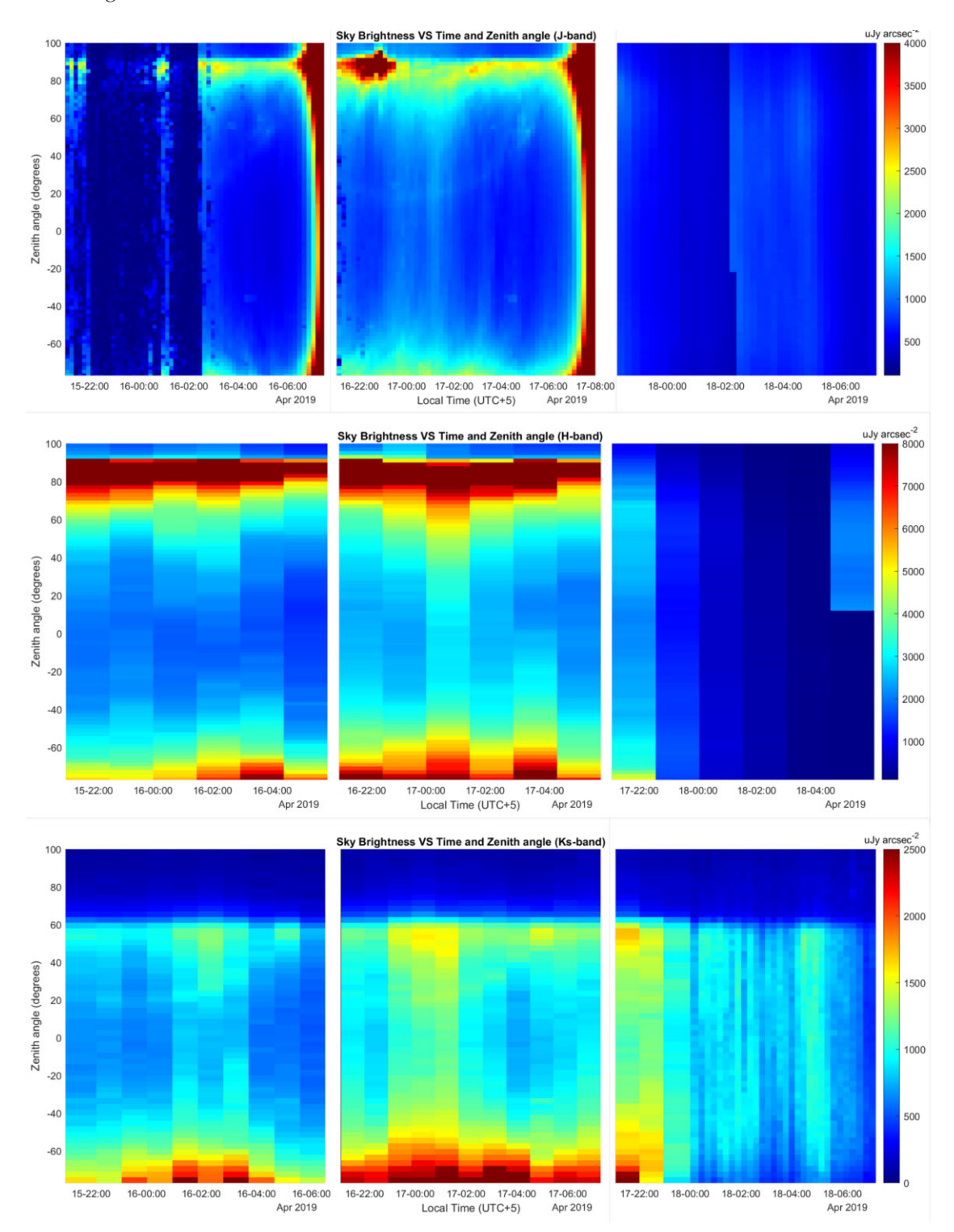


Figure 13. Sky brightness scans of intensity at zenith angles of J, H, and Ks bands from April 15–17.

points, EL1 and EL2. When the Sun's elevation is less than EL1, it is night and the sky brightness has no relationship with the Sun's elevation. When the Sun's elevation is between EL1 and EL2, it is dawn or dusk and the sky brightness increases exponentially over the Sun's elevation. This no longer holds true when the Sun's elevation is higher than EL2. From the fitting results of Fig. 16, we can get the values of EL1 in the J, H, and Ks bands, which are $EL_{1J} = -7.8^{\circ}$, $EL_{1H} = -6.2^{\circ}$, $EL_{1K} = -5.5^{\circ}$.

The brightness of the sky is dependent upon the angle of the zenith. The normalized curve is shown in Fig. 17. The sky brightness is weakest at a zenith angle of zero degrees. It increases with angle until the angle is at ground level. After that, the sky brightness becomes precipitously fainter. In the Ks band, there is an extended blackbody for calibration on-site. When the angle exceeds 50° , the blackbody will be visible to the device and the readings will become weaker. When the angle is above 90° , the snow surface around the

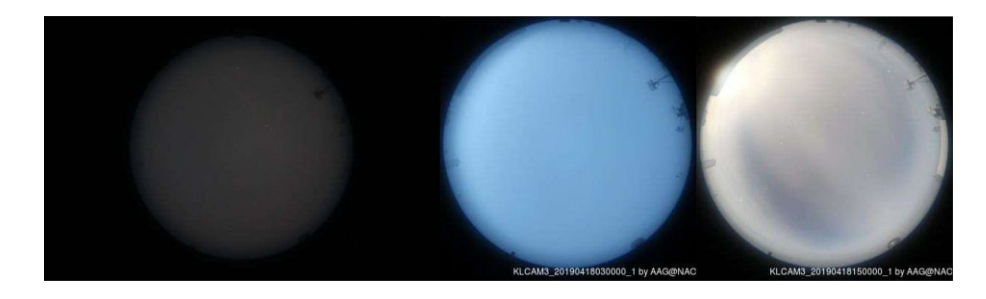


Figure 14. Picture of KLCam3 at DOME A (4.17 23:00, 4.18 3:00, 4.18 15:00).

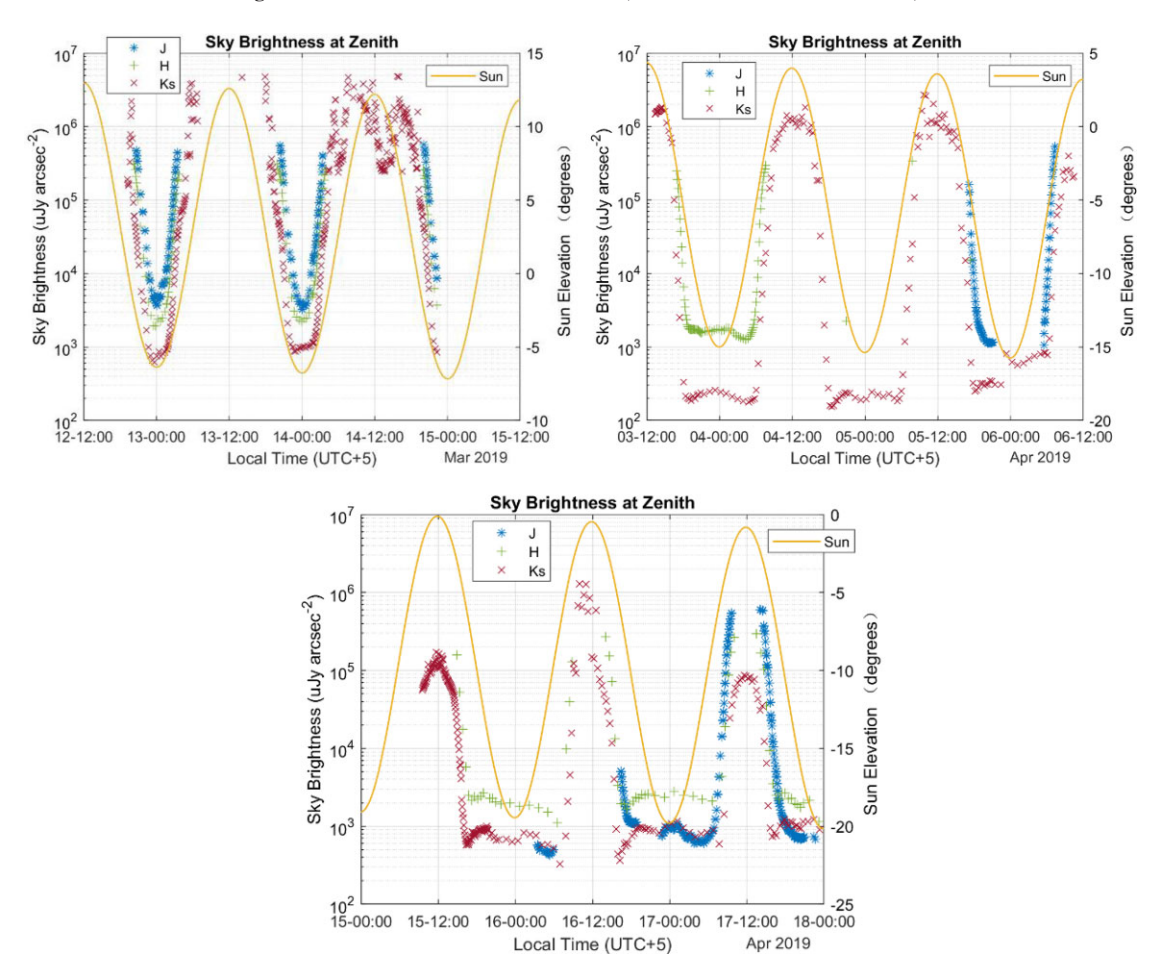


Figure 15. Variation of sky brightness of J, H, and Ks at the zenith with time (2019 March 12–15, April 3–6, and April 15–17 in local time).

station is visible to the instrument in the J and H bands, causing the value of the measurements to plunge drastically.

The radiation sources of the atmosphere are airglow and thermal emission. In the shorter wavelength band of NIR, airglow from OH dominates, while in the more extended wavelength band thermal emission from the sky begins to dominate. The atmospheric model in Phillips (1999) was employed, providing a formula for atmospheric radiation that has parameters of wavelength and angle. When airglow dominates(λ <2.3 μ m), the measured flux of sky brightness $I(\lambda, \theta)$ can be represented as follows:

$$I(\lambda, \theta) = I_{\text{OH}}(\lambda) \sec \theta e^{-\tau \sec \theta} + B(\lambda).$$
 (5)

Here, $I_{\rm OH}(\lambda)$ is the flux of OH airglow, $\tau(\lambda)$ is the observed optical depth of the atmosphere, and $B(\lambda)$ is the basic radiation of the device.

The fluxes of sky brightness in the J, H, and Ks bands are normalized and fitted for the zenith angle θ . The fitting formula is

$$I(\theta) = A \sec \theta e^{-\tau \sec \theta} + B, \tag{6}$$

with the fitted results listed in Table 8 and overplotted on the data in Fig. 18.

The fits have errors due to missing data and fluctuations in radiance from the Sun, Moon, and cloud. Even though most data were not taken in astronomical night-time darkness, we still match the formula well. According to the analysis of measured data at the zenith, the sky brightness in the three NIR bands at DOME A is calculated, as shown in Table 9, compared with Ali, Siding Spring, Mauna Kea, and the South Pole.

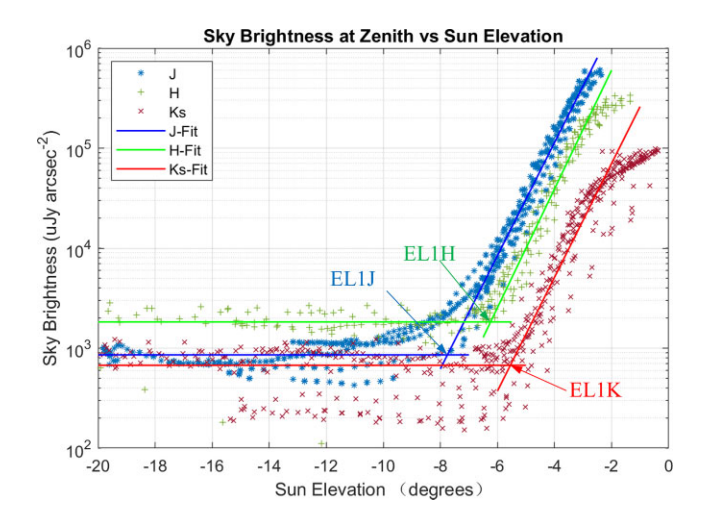


Figure 16. Plot of sky brightness in *J*, *H*, and *K*s bands versus Sun's elevation.

From the comparison in Table 9, the sky brightness in the *J* and *H* bands at DOME A is close to that at mid-latitude sites like Ali, Siding Spring, and Mauna Kea. However, the sky brightness in the *K*s band at DOME A is much darker than at those mid-latitude sites and closer to that of the South Pole.

5. CONCLUSIONS

In this work, a near-infrared sky background monitor (NISBM) based on InGaAs detectors has been presented for measurement of infrared sky brightness in the J, H, and Ks bands at night at Kunlun Station, Antarctica. The NISBM comprises three individual radiation meters, which are used to measure the intensity of near-infrared

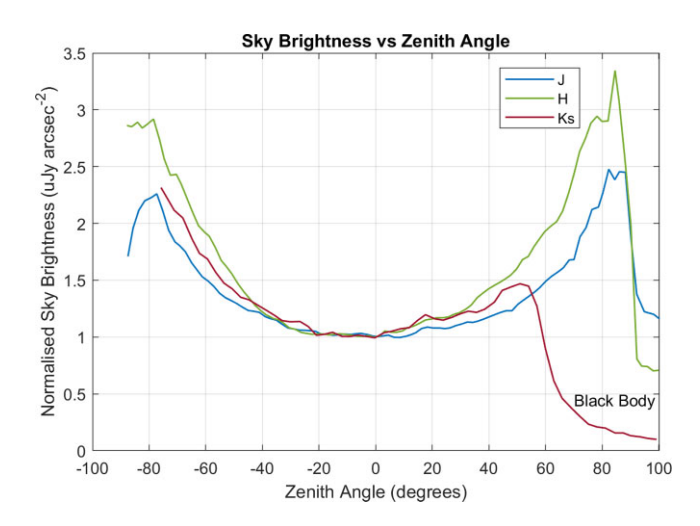


Figure 17. Normalized curve of sky brightness versus zenith angle.

Table 8. Zenith sky-brightness fitting parameter results.

Coefficient	J (1.25 μ m)	H (1.635 μm)	Ks (2.15 μm)
A	0.73±0.02	1.5±0.1	1.2±0.2
B	0.38 ± 0.04	-0.3 ± 0.1	0.0 ± 0.1
τ	0.14 ± 0.01	0.179 ± 0.006	0.19 ± 0.03

sky background radiation in the *J*, *H*, and *K*s bands separately. The straightforward design improves the trustworthiness of each machine. The *K*-band device is susceptible to background radiation, so we installed an on-site blackbody for real-time calibration to mitigate its effects. The 35th Chinese National Antarctic Research

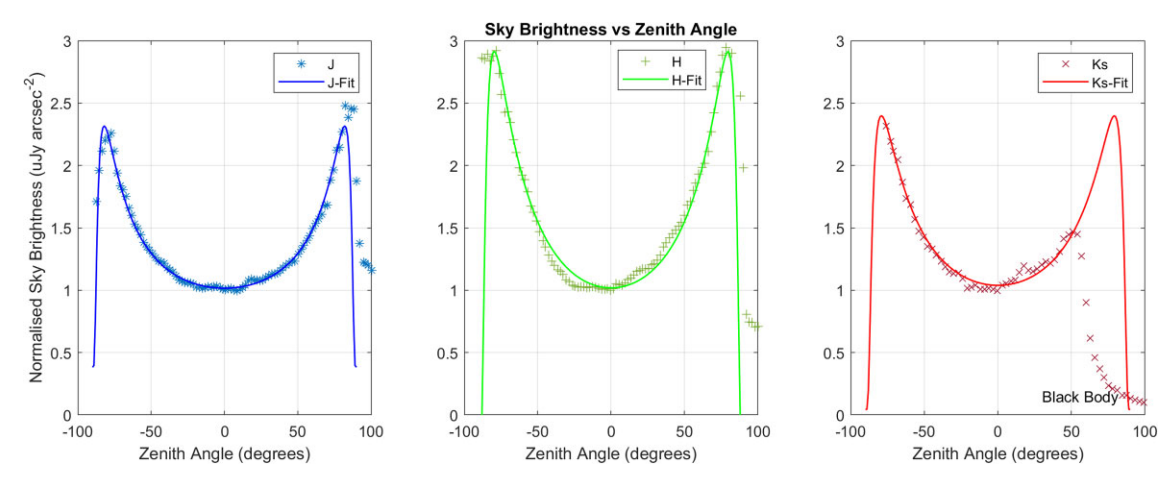


Figure 18. Fitting curve of sky brightness versus zenith angle.

Table 9. Comparison of sky brightness at zenith at different sites.

Sky brightness (μJy arcsec ⁻²)	Latitude	Altitude ⁽¹⁾ (m)	J (1.25 μm)	H (1.635 μm)	Ks (2.15 μm)
DOME A	80.4 °S	4087	600–1100	1100-2600	200–900
Ali ⁽²⁾	32.3 °N	5100	700-1100	1600-2600	800-1300
Siding Spring ⁽³⁾	31.3 °S	1165	1000-1500	1500-3000	3000-7000
Mauna Kea ⁽⁴⁾	19.8 °N	4207	~592	~3262	~843
South Pole ⁽³⁾	90 °S	2800	300-600	800-2000	~400

Notes. ⁽¹⁾ Elevation above sea level; ⁽²⁾ Tang (2018); ⁽³⁾ Phillips (1999); ⁽⁴⁾ Gemini Observatory Web, http://www.gemini.edu/observing/telescopes-and-sites/sites#Near-IR-short.

Expedition team transported the NISBM to DOME A, where it was set up and ran effectively, starting in 2019 January. For Kunlun Station, we found turning-point angles that allowed the removal of solar-radiance interference in J, H, and Ks bands: EL1_J = -7.8° , EL1_H = -6.2° , EL1_K = -5.5° ; this is a result of analysis of the correlation between the solar altitude angle and the intensity of the sky background. Compared with some higher altitude but mid-latitude sites, the Ks-band brightness of the sky at DOME A is substantially lower, nearly the same as that of the South Pole, which shows that DOME A is an excellent site for observation in Ks.

ACKNOWLEDGEMENTS

We are grateful to the 35th Chinese National Antarctic Research Expedition team supported by the Polar Research Institute of China and the Chinese Arctic and Antarctic Administration. The authors are grateful for the site installation of Zhaohui Shang at the National Astronomical Observatories and the helpfulness of data processing and remote control from Bin Ma at the National Astronomical Observatories. The authors are thankful for discussions about the optical system with Zheng-yang Li and Hai-ping Lu at the National Astronomical Observatories/Nanjing Institute of Astronomical Optics and Technology, Chinese Academy of Sciences, and Liang Chang at Yunnan Astronomical Observatories. This work was supported in part by the Fundamental Research Funds for the Central Universities (WK2360000003 and WK2030040064), in part by the National Natural Science Funds of China under Grant Nos 11603023 and 11773026, in part by Research Funds of the State Key Laboratory of Particle Detection and Electronics, in part by the SOC program (Grant No. CHINARE2017-02-04), in part by Research Funds of Key Laboratory of Astronomical Optics Technology, CAS, and in part by Research Funds of the Key Laboratory for Polar Science, MNR, Polar Research Institute of China (No. NSFC11973037).

DATA AVAILABILITY

The original data used in this work will be shared on reasonable request to the corresponding authors.

CONFLICT OF INTEREST

The authors declare no confilict of interst.

REFERENCES

Ashley M. C. B., 1995, SPIE, 2552, 33 Ashley M. C. B., 1996, PASP, 108, 721 Chen J. T., 2020, J. Astron. Telesc. Instrum. Syst., 6, 3 Lawrence J. S., 2002, PASA, 19, 328 Lawrence J. S., 2009, Rev. Sci. Instrum, 80, 064501 Ma B., 2020, Nature, 583, 771 Matthew S. R. F., 2018, PhD thesis, UNSW Nguyen H. T. 1996, PASP, 108, 718 Phillips A., 1999, ApJ, 527, 1009 Shang Z. H., 2020, Res. Astron. Astrophys., 20, 10 Sánchez S. F., 2008, PASP, 120, 873 Storey J. W. V., 1999, PASP, 111, 765 Simons D. A., 2002. PASP, 114, 169 Tokunaga A. T., 2002 PASP, 114, 180 Tang Q. J., 2018, J. Astron. Telesc. Instrum. Syst., 4, 4 Tang Q. J., 2019, J. Instrum., 14, P05011 Wang Z. Y., 2019, IEEE Trans. Nucl. Sci., 66, 8

Yang C.W., 2019, Chin. J. Polar Res. (in Chinese), 31, 2

This paper has been typeset from a T_EX/I_EX file prepared by the author.